Bioinspired, anisotropically highly thermoconductive silicon carbide/epoxy composite based on a nacre-mimetic architecture

Xiaonan Zhou
   Xi'an Jiaotong University

Jiaoqian Xu
   Xi'an Jiaotong University

Mulun Wu
   Xi'an Jiaotong University

Junjie Gao
   Xi'an Jiaotong University

Jianfei Zhang
   Xi'an Jiaotong University

Qiaogen Zhang
   Xi'an Jiaotong University

Zhongqi Shi
   Xi'an Jiaotong University

Bo Wang

   wangbo_1@xjtu.edu.cn

   Xi'an Jiaotong University

Chao Xu
   Harbin Institute of Technology

Jianfeng Yang
   Xi'an Jiaotong University

Research Article

Additional Declarations: No competing interests reported.

Abstract

Although nature's wisdom resides in achieving an exceptional functionality, such as anisotropic properties by constructing intelligently hierarchical architectures, the preparation of bulk biomimetic materials under environmental factors is still a great challenge. Inspired from the transport behavior of ions and water through the directionally aligned channels in trees, we demonstrate a facile, scalable approach to construct an anisotropic 3D biomorphic silicon carbide (bio-SiC) framework in epoxy resin (EP) matrices. The 3D bio-SiC framework has not only the highly dense elongated microchannels in the axial direction, which serves as a phonon "expressway" to facilitate thermal conduction of the whole composites, but also the robust latticed structure in the radial direction restricting the molecular chain motion. Consequently, the novel epoxy composite (bio-SiC/EP) with a nacre-mimetic architecture has a high thermal conductivity (TC) of 10.40 W m^{-1} K^{-1}, an outstanding TC enhancement efficiency of 253 per 1 vol% filler at ~ 22 vol% bio-SiC loading, together with an extremely low coefficient of linear thermal expansion (CLTE) of 12.44 ppm K^{-1} (~ 17 vol%), an excellent thermal stability, a remarkable anti-flaming performance, and a high flexural strength of 184 MPa (~ 17 vol%). Our finding gives a promising insight to achieve anisotropically highly thermoconductive polymer-based thermal management materials.

1 Introduction

Ideal packaging for modern microelectronic equipment requires an anisotropic heat dissipation via thermal management materials (TMMs) [1]. At present, the most advanced TMMs are composed of epoxy resin (EP) matrix and highly thermoconductive fillers, such as ceramic particles (Al$_2$O$_3$, BN, AlN, Si$_3$N$_4$, etc.) and carbon materials (graphite, graphene, carbon nanotubes, etc.) [2–7]. Among them, silicon carbide (SiC) has excellent mechanical properties, remarkable chemical stability, high thermal conductivity (TC) and low coefficient of linear thermal expansion (CLTE) [8–11].

In conventional methods, the melt mixing is usually used to manufacture thermoconductive epoxy composites by randomly dispersing inorganic fillers in the EP matrix due to their compatibility with current industrial practices [12]. However, TC enhancement of the epoxy composites with disorderly arranged fillers is greatly restricted owing to huge thermal resistance at the filler/filler and filler/EP interfaces and the lack of efficient heat transfer pathways [13]. Generally, the epoxy composites prepared by conventional blending methods need a large amount of highly thermoconductive filler loading (> 50 vol%) to acquire relatively low TC values (above 1 – 5 W m^{-1} K^{-1}) [14, 15]. Consequently, minimizing the filler loading in epoxy composites while realizing high TC values to get an outstanding TC enhancement still remains a huge challenge.

Construction of a 3D ordered inorganic filler network in EP matrix is considered to be an efficient strategy to obtain improved thermal properties at a very low filler loading [16–21]. This is because the 3D interconnected network can fully utilize the thermal transfer ability of fillers and serves as a "highway" for the fast transmission of phonons through the whole composite, eventually resulting in a dramatically reduced filler/EP interfacial thermal resistance [22]. For example, the epoxy composite with a 3D

interconnected BNNSs network exhibits a TC of 3.1 W m^{-1} K^{-1} with a 9.6 vol% BNNSs loading [23]. The epoxy composite with a 3D interconnected and vertically aligned graphene framework shows a TC of 2.13 W m^{-1} K^{-1} with a 0.92 vol% graphene loading [24]. The epoxy composite obtained by infiltrating 3D SiCNW networks with EP represents a TC of 1.67 W m^{-1} K^{-1} with a 2.17 vol% SiCNW loading [5].

Nevertheless, lots of works on 3D filler-network-embedded epoxy composites exhibit less satisfactory TC values, such as the maximum TC value of 3D SiC-network-embedded epoxy composites is only 1.67 W m^{-1} K^{-1} in recent years [5]. It is mainly caused by the undesired interfacial thermal resistance between loosely contacted 3D inorganic filler network, but also due to the heterogeneous architecture [25]. Firstly, the 3D inorganic particles-interconnected networks prepared by freeze-drying or self-assembly processes are heterogeneous and weak owing to Van der Waals forces and hydrogen bonds between fillers [26, 27], which leads to inefficient heat transfer between filler interconnections. On the other hand, the 3D filler foams fabricated by template methods have insufficient interconnection density, resulting in low-density heat transfer pathways in final epoxy composites [28]. All in all, the thermal conduction will inevitably become less efficient due to the presence of these structural flaws. Moreover, modern microelectronic devices also need the TMMs with low CLTE [29]. The low CLTE TMMs can reduce expansion mismatches and thermal-evoked stresses between TMMs and electronic components [30, 31]. The 3D highly covalently bonded and dense networks can successfully limit the thermal expansion of EP [32]. For instance, compared with pure PMMA, the CLTE of 3D BNFs/PMMA composite strikingly reduced by ≈ 50% at an ultra-low BNFs loading of ≈ 2.7 wt% [33]. Thus, the facile fabrication of a kind of dense and highly homogeneous 3D interconnected thermal conductive network with long-range order in polymeric composites under ambient conditions remains a major challenge.

Biological materials can inspire new alleys to design complicated and diversified materials with unique microstructures, miniaturization, functional interaction and environmental adaptability [34]. Many biological composites with unusual structures can be found in nature, such as the vertically aligned mineral collagen/enamel prism in teeth, and the "brick and mortar" architecture in the nacre both lead to their good multifunctional properties [35, 36]. Learning from nature, artificial composites can be reasonably designed to acquire the desired performance. As a nice example, highly oriented arrangement of graphite crystallites at EP matrix can strikingly enhance TC of 3D graphite/EP composite because of the aligned architectures [37]. However, it is difficult for fillers to form continuous heat transfer channels along the arrangement direction, resulting in the inevitable weakening of heat conduction. Moreover, expensive raw materials and complex preparation process also hinder the expansion of these materials. More careful material selection and more rational process design are needed to further improve the ordered structures of 3D filler network and the excellent properties of its composite.

Inspired from the transport behavior of ions and water through the directionally aligned channels in trees during photosynthesis and transpiration, the 3D hierarchically porous structure with highly dense elongated microchannels is perfect for architecting a thermal conductive "expressway" in polymer-based composite. Herein, we propose a wood-derived replica technique to construct a robust 3D biomorphic

SiC (bio-SiC) network, which has latticed structure in the radial direction and highly dense elongated microchannels in the axial direction, respectively. Therefore, the 3D nacre-mimetic architecture with vertically aligned bio-SiC microchannels exhibits an excellent TC enhancement on EP matrix, typically endowing the obtained epoxy composite (bio-SiC/EP) with a high TC of 10.40 W m^{-1} K^{-1} (~ 22 vol%). Together with its an outstanding TC enhancement efficiency of 253 per 1 vol% loading. We expect this study could open up a new path to boost the development of 3D ceramic network/polymer composites.

2 Experimental Section

2.1 Materials

Spruce wood was offered by Guiyang Wood Factory Co., Ltd, China. Silicon monoxide (SiO) particles were offered by Shanghai Chaowei Nano Technology Co., Ltd, China. Ethyl alcohol and acetic acid were offered by Sinopharm Chemical Reagent Co., Ltd, China. Bisphenol-A EP (E51, DGEBA) was purchased from Shanghai Resin Factory Co., Ltd, China. 3-glycidoxypropyltrimethoxy silane (KH-560), 2,4,6-tris(dimethylaminomethyl)phenol (DMP-30) and methyltetrahydrophthalic anhydride (MeTHPA) were offered by Shanghai Macklin Biochemical Technology Co., Ltd, China.

2.2 Preparation of bio-C template

Firstly, the natural spruce wood (size: 50 mm × 50 mm × 50 mm) was dried at 100 °C for 24 h. After that, the specimens were pyrolyzed at 1000 °C for 4 h under N_2 atmosphere to prepare bio-C templates, the heating rate from room temperature to 500 °C was 0.5 °C min^{-1} and 2 °C min^{-1} for 500 to 1000 °C.

2.3 Preparation of 3D bio-SiC network

Firstly, the SiO particles and bio-C templates were put into a closed graphite crucible. After that, the crucible was put into a multifunctional sintering furnace and sintered at 1800 °C for 4 h under Ar atmosphere to prepare 3D bio-SiC networks, the heating rate from room temperature to 1200 °C was 20 °C min^{-1} and 5 °C min^{-1} for 1200 to 1800 °C.

2.4 Preparation of bio-SiC/EP composite

The alcohol and water (mass ratio of alcohol: water = 95: 5) were evenly mixed at 60 °C for 10 min in a water bath. Then the KH-560 (0.57 wt% of alcohol/water mixture) was added to the alcohol/water mixture to prepare a hydrolysis solution. Subsequently, the 3D bio-SiC networks were soaked in the mixture at 80 °C for 3 h, and the specimens were dried at 80 °C for 24 h. The EP was then well mixed with the accelerator and the curing agent at 60 °C for 30 min (mass ratio of DMP-30: MeTHPA: EP = 1: 86: 100). After that, the functionalized 3D bio-SiC frameworks were immersed for 4 h under vacuum into the resulted mixture. Finally, the bio-SiC/EP composites were cured at 80 °C for 2 h and 150 °C for 6 h.

2.5 Measurement and characterization

The Archimedes drainage method was used to determine the porosity and density of the specimens. A field emission scanning electron microscope was used to examine the morphological of the specimens (FESEM, Zeiss GeminiSEM 500, Germany). The functional groups of the specimens were characterized using Fourier transform infrared (FTIR, Bruker VERTEX70, American). The specimens were subjected to X-ray diffraction analyses using an X-ray diffractometer (XRD, PANalytical X'Pert PRO, Netherlands). A laser-flash diffusivity instrument was used to measure the TC of the specimens (Netzsch LFA467, Germany). An IR camera was used to capture the thermographic figures of the specimens (Fotric 285, China). A thermomechanical analyzer was used to measure the CLTE values of the specimens (TMA, Netzsch DIL 402 C, Germany). A thermal gravimetric analyzer was used to perform the thermal stability of the specimens (TGA, TA SDT Q600, American). An universal testing machine was used to determine the flexural strength of the specimens (UTM 2103, China).

3 Results And Discussion

The wood-carbon-ceramic-composite's design idea and straight forward top-down preparation procedure of the bio-SiC/EP composites are illustrated in Fig. 1a. We choose spruce wood as the raw material due to its unusual structure, consisting of anisotropic and highly dense elongated microchannels. The original natural wood can be easily transformed into biomorphic carbon (bio-C) template by carbonization at high temperature. After that, the porous bio-SiC ceramic was synthesized by the carbothermal reduction (CR) reaction of bio-C template on the basis of the equation: $2C(s) + SiO(g) \rightarrow SiC(s) + CO(g)$. Subsequently, liquid EP was penetrated into the functionalized 3D bio-SiC framework and then thermal curing to form dense bio-SiC/EP composite with "brick and mortar" architecture. Different from loosely contacted 3D filler networks, a monolith of a 3D bio-SiC network was fabricated by our approach, in which heat energy can move rapidly through the high-quality and continuous bio-SiC microchannels. Therefore, we expect to observe extraordinary thermal properties of bio-SiC ceramic and bio-SiC/EP composite.

Figure 1b display the optical images of natural spruce wood, bio-C templates, bio-SiC ceramics and bio-SiC/EP composites. A clear linear shrinkage (22.8 – 33.1%) occurs during pyrolysis processing [38]. Whereas, the macro-characteristics (such as the annual growth rings) of nature spruce wood are still obviously visible in the bio-C templates. Comparing with the bio-C templates, the bio-SiC ceramics maintain the macro-shape after CR at 1800 °C for 4 h, and without cracks or other defects are visible in the bio-SiC ceramics. The only variation seen is the body color transition from black to light green, suggesting that the CR happened. After EP infiltration, dense bulk samples with smoother surface can be observed, and the body color of the bio-SiC/EP composites becomes dark. It should be mentioned that the spruce wood can be easily tailored into different sizes and shapes on the basis of the application scenarios. In addition, the advantages of facile preparation process and low-cost raw materials can ensure the wide application of the bio-SiC/EP composites.

Figure 2 exhibits the microstructure of the anisotropic bio-C template, bio-SiC ceramic and bio-SiC/EP composite. As shown in Fig. 2a, a dense, highly anisotropic architecture is exhibited in the micro-CT image of bio-SiC/EP composite. Without clear micropores are found in the composite, suggesting the well adhesion of the bio-SiC/EP interface. Highly porous, interconnected 3D bio-SiC skeleton, similar to the original bio-C template carbonized from nature wood, embedded in the EP matrix could be clearly shown in the white section. The microstructures of composite at different regions are consistent in two dimensions, indicating a good homogeneity of the bio-SiC/EP composite, as shown in Fig. 2b – e.

Generally, the spruce wood possesses latticed structure and long aligned channels in the cross-sections of axial direction and radial direction, respectively. Interestingly, although large shrinkage occurs, the unique hierarchical structures can be perfectly preserved even after pyrolysis at high temperature. As shown in Fig. 2f, the obtained bio-C template almost completely maintains the latticed structure of the spruce wood, comprising numerous lattice-shaped subunits of 20 – 40 µm. The cross-section of radial direction shows a vertically aligned channels with very thin channel wall of 2 – 3 µm, which inherits the microstructure of the spruce wood, including the aligned long channels that grow through the whole tree for the transport of ions and water during photosynthesis and transpiration (Fig. 2j).

After fully CR at 1800 °C for 4 h, the obtained bio-SiC ceramic inherits the microstructure of the bio-C template, including the latticed structure of 20 – 40 µm and the thin channel wall of 2 – 3 µm (Fig. 2g, k). The homogeneous vertically aligned long channels ensure the reaction of the solid C inside bio-C templates and the SiO gaseous produced by SiO particles, this results in a spatially uniform phase transition. It is worth noting that the cell wall of the as-obtained bio-SiC ceramic has a few visible micropores, which are generated due to the volume shrinkage during phase transformation processing from C to SiC (Fig. 2k).

The cross-section microstructure of bio-SiC/EP composite in the axial direction is shown in Fig. 2h. A perfect "brick and mortar" architecture can be obtained by CR of bio-C template derived from nature wood followed by EP infiltration. After EP infiltration, the cells are completely filled with EP, and the bio-SiC/EP composite is composed of two interpenetrating networks. Generally speaking, the unique structures of biological materials determine their properties, and the multiscale structures are difficult to copy comprehensively. Our researches suggest that, by adjusting the CR reaction and the adhesion at the inorganic/organic layer interface, multiscale microstructure characteristics can also be established to improve the thermal properties of the final materials (such as heat dissipation and structural reinforcement). The mapping of the bio-SiC/EP composite by energy-dispersive spectroscopy (EDS) demonstrates that Si is uniformly distributed throughout the cell walls, indicating a perfect inheritance from the original natural wood by the fully CR reaction (Fig. 2i). The cross-section microstructure of bio-SiC/EP composite in the radial direction is shown in Fig. 2l. A distinct "cross-lamellar" microstructure is obtained, where EP layers are held together by inorganic "glue" (bio-SiC ceramic). The well-defined layered architecture is similar to the structure of conch shell, which would contribute to high toughness

of the composite. Usually, the original bio-SiC ceramic surface does not wet with EP. However, after surface functionalization, the 3D bio-SiC framework shows a good wettability with EP after infiltration under vacuum, demonstrating the full EP infiltration in the vertically aligned channels. The EDS mapping of bio-SiC/EP composite also indicates that the element of Si is evenly distributed throughout the channel walls, indicating the full phase transformation from C to SiC (Fig. 2m).

The microstructure of inorganic wall and the inorganic/organic interface are key contributors to the final properties of composites. FTIR spectra of raw bio-SiC ceramic and modified bio-SiC ceramic are presented in Fig. 3a. The characteristic peak at 841 cm^{-1} is assigned to the Si-C stretching vibration, which confirms the existence of SiC. In addition, two characteristic bands centered at 777 and 1053 cm^{-1} are attributed to the stretching vibrations of the Si-O and Si-O-Si bonds, respectively. It was due to the formation of natural silicon dioxide (SiO_2) oxide layer on the bio-SiC ceramic surface. Compared with raw bio-SiC ceramic, modified bio-SiC presents new peaks at 2850, 2921 and 2950 cm^{-1}, this is due to the aliphatic C-H valence stretching vibration. After surface modification, EP groups had been successfully introduced to the surface of 3D bio-SiC framework. Figure 3b shows XRD patterns of bio-SiC/EP composites. There are five typical peaks at 2θ = 35.3, 41.2, 59.8, 71.6 and 75.3°, which match the (111), (200), (220), (311) and (222) crystal planes of the cubic type β-SiC phase, respectively, which confirm the high crystallinity and high purity features of bio-SiC ceramic.

Figure 3c shows a representative microstructure of the etched bio-SiC ceramic. The highly dense and homogeneous distribution bio-SiC columnar nanocrystals (length of ~ 800 nm, width of ~ 200 nm) in the cell wall are clearly visible. The initial structural directionality of the cellulose nanofibers in the trees is copied into this microstructure [39]. The highly dense elongated microchannels contribute to achieve outstanding thermal properties of the 3D bio-SiC network. Figure 3d indicates a high magnification SEM photograph of the bio-SiC/EP composite, the strong interfacial bonding between 3D bio-SiC network and EP can be observed. This is because the EP groups of the functionalized bio-SiC can enhance the compatibility of bio-SiC and EP by introducing stronger covalent bonds, enhancing the interfacial interactions. Figure 3e, f show the microstructures of unmodified bio-SiC/EP composite and the interface between unmodified bio-SiC and EP, respectively. The SEM micrograph obviously exhibited a weak interfacial bonding between the SiC/EP interface (Fig. 3e). As shown in Fig. 3f, large gap between SiC and epoxy could be clearly observed, reflecting weak interfacial adhesion between inorganic filler and polymer. It was due to the adhesion force was lower than the inevitably shrinkage force of epoxy during curing processing. These results indicate that the surface modification of fillers is a key step for fabricating the polymer-based composites [18].

To study the relationship between anisotropic structure and TC of the bio-SiC ceramics and the bio-SiC/EP composites, the TC of axial direction ($k_{//}$) and radial direction ($k_\perp$) were characterized. The

relationship between TC and relative density of the bio-SiC ceramics is shown in Fig. 4a. The TC values of bio-SiC ceramics in two orientations both exhibit a considerable improvement with increasing relative density. The $k_{//}$ of bio-SiC ceramics increases from 2.84 to 10.26 W m^{-1} K^{-1}, and the $k_{\perp}$ increases from 1.59 to 7.65 W m^{-1} K^{-1} with the relative density increasing from ~ 11 to ~ 24%, which is due to the increase in the number of heat transfer paths. In addition, anisotropic TC can be observed because of the unusual anisotropic microstructure of bio-SiC ceramics, and the $k_{//}$ is higher than the $k_{\perp}$. With an increasing porosity from 78 to 88%, the anisotropic TC ratio ($k_{//}/k_{\perp}$) in bio-SiC ceramics slightly increases from 1.55 to 2.24.

The TC of bio-SiC/EP composites presented the same trend compared with the bio-SiC ceramics (Fig. 4b). With an increasing filler loading from 10 to 24 vol%, the $k_{//}$ of bio-SiC/EP composites increases from 3.43 to 10.40 W m^{-1} K^{-1}, the $k_{\perp}$ of bio-SiC/EP composites increases from 1.18 to 7.80 W m^{-1} K^{-1}, suggesting that the existence of 3D bio-SiC network leads to a significant TC enhancement of the EP. A similar of anisotropic TC ratio ($k_{//}/k_{\perp}$) of 1.55 – 2.03 in composites could be achieved. As shown in Fig. 4b, the $k_{//}$ of unmodified 16-bio-SiC/EP composite and 16-bio-SiC/EP composite slightly increase to 5.57 and 5.40 W m^{-1} K^{-1} comparing to that of 16-bio-SiC ceramic (5.28 W m^{-1} K^{-1}), respectively. This is due to the higher TC value of EP matrix (~ 0.18 W m^{-1} K^{-1}) comparing with that of air (~ 0.03 W m^{-1} K^{-1}). The above results suggest that the TC of bio-SiC/EP composite is mostly supplied by the densely interconnected 3D bio-SiC network. Consequently, the interfacial thermal resistance between SiC/EP interface has a negligible effect on the TC of bio-SiC/EP composites, which is largely determined by the interfacial thermal resistance between SiC/SiC interface. To calculate it, we applied a nonlinear physical model proposed by Foygel et al. (Equation S1) [40]. After the tangent on the experimental data curve was determined, the values of V_c (16.66 vol%) for the bio-SiC$_{//}$/EP composites and V_c (18.25 vol%) for the bio-SiC$_{\perp}$/EP composites were obtained (Figures S1 and S2). The values of K_0 (1.45 W m^{-1} K^{-1}) and τ (0.35) for the bio-SiC$_{//}$/EP composites were then derived by fitting the experimental data (Fig. S3). For the bio-SiC$_{\perp}$/EP composites (Fig. S4), the values turn to K_0 (1.19 W m^{-1} K^{-1}) and τ (0.25). Then, the contact resistance (R) between bio-SiC nanocrystals was calculated by the Equation S2 using the parameters. The R of 1.61 × 10^6 K W^{-1} for the bio-SiC$_{//}$/EP composites and 1.62 × 10^6 K W^{-1} for the bio-SiC$_{\perp}$/EP composites are obtained. It is worth noting that the R of bio-SiC/EP composites are lower than the 3D BN/EP composites prepared by freeze-drying and infiltration of polymer matrix (Table S1) [27]. This is because highly dense 3D bio-SiC framework could be achieved owning to the volume expansion during phase transformation from C to SiC in our study (Fig. 3c), leading to a significantly reduced filler/filler interfacial thermal resistance and achieving high TC. The temperature-dependent TC of 22-bio-SiC$_{//}$/EP composite, 24-bio-SiC$_{\perp}$/EP composite and pure EP is shown in Fig. 4c. These TC values remain almost unchanged from 25 to 100 °C, which indicates that the heat transfer ability is stable. The long-term performance of equipment will benefit from such a slight temperature-dependent change in TC.

The TC values of the bio-SiC$_\parallel$/EP composites are compared to that of other epoxy composites reinforced by different 3D interconnected ceramic networks, such as BN, Si$_3$N$_4$, Al$_2$O$_3$, AlN and so on (Fig. 4d) [17, 27, 41–45]. The maximum TC of 10.40 W m^{-1} K^{-1} in bio-SiC$_\parallel$/EP composites is achieved with ~ 22 vol% bio-SiC, displaying ≈ 58 times larger numbers than that of pure EP (~ 0.18 W m^{-1} K^{-1}). Such TC value is far beyond other inorganic filler-contained EP composites with similar filler loading, such as 3D Si$_3$N$_4$/EP of 3.89 W m^{-1} K^{-1}, 3D BN/EP of 4.42 W m^{-1} K^{-1}, 3D Al$_2$O$_3$/EP of 3.17 W m^{-1} K^{-1}, and 3D AlN-H/EP of 9.48 W m^{-1} K^{-1} reported previously (Table S2). The outstanding thermal conduction performance for our composites results from the formation of phonon-matching 3D bio-SiC networks, resulting in high rates of phonon transport in the vertically aligned channels. The TC enhancement efficiency for 3D bio-SiC skeleton in EP is characterized by enhancement per 1 vol% loading (η), which is defined as

$$\eta = \frac{K - K_m}{100 V_f K_m} \times 100\%$$

1

where K and K_m are the TC of the composites and EP, respectively, and V_f is the loading of bio-SiC in composites. We compared the η of 22-bio-SiC$_\parallel$/EP composite and 24-bio-SiC$_\perp$/EP composite with other composites are shown in Fig. 4e, and the detailed data are listed in Table S2 [8, 17, 19, 27, 41–49]. The η of bio-SiC$_\parallel$/EP composite reaches 253 as the filler loading of ~ 22 vol%, which is higher than bio-SiC$_\perp$/EP composite with ~ 24 vol% filler loading (179). The latticed structure in the axial direction and long aligned channels in the radial direction resulted in the anisotropic enhancement efficiency and relative higher η value. The outstanding enhancement efficiency is far beyond other 3D ceramic/EP composites. Comparing with the 3D SiC/EP composites fabricated by other techniques, much higher η was achieved in the current study due to the higher density of 3D bio-SiC framework.

The heat dissipation profiles of 15-bio-SiC ceramics and its composites in two directions are identified by an infrared camera. The pure EP, 15-bio-SiC ceramics and 15-bio-SiC/EP composites with the same thickness (≈ 2 mm) and size (10 mm × 10 mm) are placed on a heater and then heated at room temperature simultaneously as shown in Fig. 5a. The surface temperature of bio-SiC$_\parallel$ ceramic increases much faster than bio-SiC$_\perp$ ceramic with time for the 15-bio-SiC ceramics. Moreover, the 15-bio-SiC/EP composites exhibit a similar trend, but their surface temperatures increase much faster than that of pure EP, which is in accordance with their TC. These results also demonstrate anisotropic thermal properties. In addition, the surface temperatures of 15-bio-SiC ceramics and 15-bio-SiC/EP composites increase at nearly the same rate in the same direction because of their similar TC. Such characteristics demonstrate again that the 3D bio-SiC frameworks nearly entirely provide the heat transfer capacity of bio-SiC/EP composites. The results are also confirmed by the top surface temperature-heating time curves that can be observed in Fig. 5b. As shown in Fig. 5c, after heating for 30 s, the top surface temperature of 15-bio-SiC$_\parallel$/EP composite is as high as 82 °C. However, the top surface temperatures of other specimens are lower than 80 °C, and that of pure EP is only 48 °C.

Finite element simulations were performed by COMSOL Multiphysics 5.4 to further research the heat transfer process of bio-SiC/EP composites (Fig. 6, the specific parameters are shown in Supporting

Information S2). Figure 6a – c illustrate the temperature distribution of pure EP, 20-bio-SiC$_\perp$/EP composite and 20-bio-SiC$_\parallel$/EP composite along with time, which can represent the thermal conduction velocity of materials (The dynamic changes are illustrated in Fig. S5). As shown in Fig. 6a, the heat transfers slowly and uniformly from the bottom to the top due to the low TC of pure EP. The average top surface temperature of pure EP is still unchanged throughout the process (Fig. S6a). While for 20-bio-SiC/EP composites, the heat transfers comparatively and fast from the bottom to the top (Fig. 6b, c). As shown in Fig. 6d, the heat flux of each zone in pure EP is equal. The heat flux arrows are mostly distributed in bio-SiC area but for 20-bio-SiC/EP composites, suggesting that most of the heat is rapidly transferred through the 3D bio-SiC framework (Fig. 6e, f). Due to the high TC of bio-SiC, the heat is effectively dispersed along the microchannel alignment direction, where it is carried away by forced thermal convection.

Figure 6b shows a schematic of the 20-bio-SiC$_\perp$/EP composite, where the long microchannel alignment direction is perpendicular to the input heat flux. As shown in it, the input heat is transferred upward layer by layer along the microchannel wall of bio-SiC. The heat pathway perpendicular to the microchannel wall is tortuous and complicated, the temperature section for this direction of the composite at 0.001 s is shown in Fig. 6e. While for the 20-bio-SiC$_\parallel$/EP composite (Fig. 6c), the average top surface temperature quickly approaches the bottom surface temperature, which indicates the excellent heat transfer behavior of the bio-SiC$_\parallel$/EP composite. The average temperature variations of the top surface are also recorded and shown in Fig. S6a. At the same time point, the overall temperature of the 20-bio-SiC$_\parallel$/EP composite is higher than the 20-bio-SiC$_\perp$/EP composite. The top surface temperature values of pure EP, 20-bio-SiC$_\perp$/EP composite and 20-bio-SiC$_\parallel$/EP composite are 20, 69 and 106 °C at 0.003 s, respectively (Fig. S6b). This is consistent with the test results of TC and infrared thermal imaging. Figure 6f shows the temperature section for the 20-bio-SiC$_\parallel$/EP composite at 0.001 s, where the long microchannel alignment direction is parallel to the input heat flux. As shown in it, the input heat is quickly and directly transferred upward through the microchannel wall of 3D bio-SiC framework from bottom to top surface, suggesting that the heat pathway parallel to the microchannel wall is more effectively.

The dimensional stability is a crucial characteristic for TMMs, which is usually evaluated by the CLTE value [26, 50]. The CLTE curves of pure EP, 17-bio-SiC ceramics and 17-bio-SiC/EP composites as a function of temperature are illustrated in Fig. 7a. The CLTE values of pure EP increases monotonically with temperature until ~ 120 °C, and then it considerably increases to ~ 103 ppm K^{-1}, which is because of an increase in segmental mobility as a result of the polymer chain motion state alterations. While for 17-bio-SiC ceramics, the CLTE values (~ 3 ppm K^{-1}) remain constant in the entire procedure. In addition, the CLTE values of 17-bio-SiC/EP composites close to that of 17-bio-SiC ceramics and are much less than that of pure EP. It can be explained by the interconnected 3D bio-SiC network stabilizing the entire architecture of the epoxy composites. The CLTE values of 17-bio-SiC/EP composites slightly increase at ~ 120 °C due to the increase of polymer chain segmental mobility. The CLTE values of 17-bio-SiC$_\parallel$/EP composite and 17-bio-SiC$_\perp$/EP composite increase to 19.05 and 14.05 ppm K^{-1} at 120 °C as shown in

Fig. 7b, respectively. However, pure EP presents a much higher CLTE of ~ 66.31 ppm K^{-1} at 120 °C, which indicates that the higher the temperature, the more obvious the constraint effect of the 3D bio-SiC framework. Moreover, the 17-bio-SiC/EP composites possess anisotropic CLTE, and the anisotropic CLTE ratio is 1.36.

The CLTE values of the 17-bio-SiC/EP composites are compared to that of other epoxy composites as shown in Fig. 7c [26, 27]. As shown in it, the CLTE values of 3D filler/EP composites are lower than that of random filler/EP composites, which indicates that the 3D filler framework has a better restraint on the volume expansion of EP. In our study, the 17-bio-SiC$_\perp$/EP composite possesses a much lower CLTE value of 12.44 ppm K^{-1} than that of 3D BN/EP composite (22.70 ppm K^{-1}) and 3D BNNS/EP composite (24.00 ppm K^{-1}). It indicates that the 3D bio-SiC framework with latticed structure, high shear modulus and bulk modulus, and the good interfacial adhesion between bio-SiC and EP all contribute to the decrease of CLTE of composite. In order to investigate the impact of 3D bio-SiC framework on CLTE in more detail, the theoretical CLTE values of 17-bio-SiC/EP composite are calculated by three common models: Rule of Mixture (ROM), Turner and Kerner (Equations S3, S4 and S5) [51, 52]. As shown in Fig. 7c, the theoretical CLTE values from the models (ROM: 55.79 ppm K^{-1}, Kerner: 34.01 ppm K^{-1}, Turner: 32.00 ppm K^{-1}) are substantially larger than the experimental CLTE values (12.44 and 15.04 ppm K^{-1}). These models are usually used to deduce the CLTE values of composites with similar modulus and zero internal stress. However, there is internal stress due to the significant difference in CLTE values between the 3D bio-SiC framework and EP for our composites, which enhances the stability of EP system.

Finite element simulations were performed by COMSOL Multiphysics 5.4 to interpret the internal stress and anisotropy of bio-SiC/EP composites during thermal expansion process. The distribution of thermal stress and linear expansivity of a single unit are shown in Fig. 7d. As shown in it, the 3D bio-SiC network and EP interface has the greatest thermal stress. The linear expansivity in each direction can be calculated on the basis of the average displacement of each surface of the model in Table S3. In the z direction, the linear expansivity (0.0047%) is larger than that in the x and y directions (0.0030 and 0.0046%). Similar tendency is observed for the model of multiple units (Fig. 7e). As shown in it, the linear expansivity of the 20-bio-SiC/EP composite in the z direction (0.002124%) is also higher than that in the x and y directions (0.001623 and 0.001953%). This is because the bio-SiC cell wall inhibits the volume expansion of EP under normal stress in the x and y directions, and the force of each cell wall is superimposed. While in the z direction, the bio-SiC cell wall restrains the volume expansion of EP under shear stress, and the force of each cell wall is independent. These results indicate that the bio-SiC/EP composites are anisotropic during thermal expansion process. Usually, heat sinks used for thermal management of electronic equipment often require high TC in the longitudinal direction and CLTE matching with chips and substrates in the lateral direction [53]. Consequently, the bio-SiC/EP composites combine with high TC (10.4 W m^{-1} K^{-1}) in the axial direction and low CLTE (12.44 ppm K^{-1}) in the radial direction, which is similar to the CLTE of Si chips (2.50 ppm K^{-1}) and ceramic substrates (Si$_3$N$_4$ of 3.00 ppm K^{-1}, AlN of 4.50 ppm K^{-1}), are expected to be used as heat sinks.

Thermal stability is a key factor for TMMs [54]. Figure 8 shows the TGA and DTG curves of pure EP and bio-SiC/EP composites. As shown in Fig. 8a, TGA curves of pure EP and bio-SiC/EP composites exhibit two-stage degradation behavior. The first stage happens at the temperature between about 270 and 470 °C, which is because of the decomposition of the oxygen-containing groups [55]. The second stage occurs from 470 to 620 °C, which is because of the pyrolysis of the carbon-containing groups [56]. In addition, thermal stability is greatly elucidated by the temperature at 10 wt% loss of the specimens ($T_{10\%}$). The $T_{10\%}$ of pure EP is 361.8 °C as shown in the inset of Fig. 8a, the $T_{10\%}$ increases from 377.2 to 382.2 °C as the bio-SiC loading increases from 12 to 22 vol%. It shows that the inclusion of bio-SiC can delay the degradation of EP, and the bio-SiC/EP composites become more thermally stable with increasing bio-SiC loading. The temperature corresponding to the fastest rate of degradation (the peak of DTG profile) of the bio-SiC/EP composites exhibits a similar trend as shown in Fig. 8b, and increases with increasing the bio-SiC loading. The fastest rate of degradation occurs at 405.3 °C for the 22-bio-SiC/EP composite, which is 10 °C higher than the pure EP (395.3 °C). The above results indicate that the 3D bio-SiC framework has a barrier effect, thereby improving the thermal stability of the epoxy composite [57, 58].

Generally, pure EP presents a very poor thermal stability (Fig. 8) and easily burns in air because of the oxygen-containing groups, greatly limiting its application in certain extreme circumstances [59, 60]. Therefore, the anti-flaming performance of pure EP and 17-bio-SiC/EP composite were comparatively studied (Fig. 9). As shown in Fig. 9a, upon exposure to flame, the pure EP began to shrink and deform gradually with prolonged treatment time, and completely burnt off after burning for 45 s. While for the 17-bio-SiC/EP composite, the flame gradually went out with prolonged treatment time, which is because the EP matrix was burnt out. In addition, after burning for 135 s, the 17-bio-SiC/EP composite could keep its original structure without any deformation and shrinkage (Fig. 9c). This is because the entire architecture of the bio-SiC/EP composite was stabilized by the densely interconnected 3D bio-SiC network. More obvious contrasts about shape and size can be found in infrared thermal images (Fig. 9b, d). These results indicate that the 3D bio-SiC network is easily recycled from its epoxy composite, and may be reliably reutilized for multifunctional reuse [32]. Therefore, the 3D bio-SiC network reinforced polymer (paraffin or stearic acid) composites combine with high TC are expected to be used as thermal energy storage materials.

Figure 10 shows the flexural strengths of pure EP, unmodified 16-bio-SiC$_\perp$/EP composite and 17-bio-SiC/EP composites. The flexural strength of 17-bio-SiC$_{||}$/EP composite (184 MPa) is increased by 72% as the load perpendicular to the highly dense elongated microchannels comparing with that of pure EP (107 MPa). This result indicates that the load is transferred from the EP matrix to the robust 3D bio-SiC skeleton, improving the flexural strengths of the bio-SiC/EP composites. The flexural strength of axial direction ($\sigma_{||}$ = 184 MPa) is considerably higher than that of radial direction ($\sigma_\perp$ = 122 MPa). Contrast to conventional isotropic polymer composites, the anisotropic microstructure of 3D bio-SiC framework leads to a anisotropic σ ratio ($\sigma_{||}/\sigma_\perp$) of 1.51. The strength of 3D bio-SiC skeleton is largely governed by their defect distribution, when the load is parallel to microchannels, large micropores (20 – 40 µm) would

result in low strength. However, few defects exist on the surface of highly dense elongated microchannels, leading to improved strength as the load perpendicular to microchannels. Whereas, although the filler content is similar, the flexural strength of unmodified 16-bio-SiC$_\perp$/EP composite (69 MPa) is much lower than that of 17-bio-SiC$_\perp$/EP composite (122 MPa). The existence of large gap between bio-SiC/EP interface deteriorates its mechanical properties. On the other hand, the weak interfacial interactions between bio-SiC and EP can not support the load transfer from the EP matrix to the robust 3D bio-SiC skeleton. These results indicate that the status of interfacial adhesion between filler/polymer interface has a great influence on the mechanical properties of 3D ceramic skeleton reinforced composites.

4 Conclusion

In summary, bio-SiC/EP composite was fabricated by introducing a robust 3D bio-SiC framework via a wood-derived replica technique and subsequently infiltrated with epoxy resin, in which the latticed structure in the radial direction and the highly dense elongated microchannels in the axial direction are embedded in the epoxy resin matrix, respectively. Benefiting from this unusual architecture, the prepared epoxy composite exhibits a high TC of 10.40 W m^{-1} K^{-1} (~ 22 vol%), corresponding to an outstanding TC enhancement efficiency of 253 per 1 vol% bio-SiC, suggesting a much higher value of enhancement efficiency comparing with other reported epoxy composites. The bio-SiC/EP composite possesses a low CLTE of 12.44 ppm K^{-1} (~ 17 vol%), a good anti-flaming performance (~ 17 vol%), and a high thermal stability (~ 22 vol%), which is due to a barrier effect of the 3D bio-SiC network. In addition, it also exhibits an ultra-high flexural strength of 184 MPa (~ 17 vol%), demonstrating that the load from the epoxy resin matrix can be carried by the 3D bio-SiC network. This work opens up a new path to attain anisotropically highly thermoconductive TMMs by constructing efficient nacre-mimetic 3D conductive networks.

Declarations

Supplementary Information The online version contains supplementary material available at

Author contribution Xiaonan Zhou: Investigation, Data curation, Software, Formal analysis, Methodology, Writing-original draft. Jiaoqian Xu: Data curation, Formal analysis, Methodology. Mulun Wu: Data curation, Formal analysis. Junjie Gao: Data curation, Methodology. Jianfei Zhang: Investigation, Formal analysis, Writing-original draft. Qiaogen Zhang: Writing-review and editing. Zhongqi Shi: Writing-review and editing. Chao Xu: Conceptualization, Supervision, Validation, Project administration, Writing-review and editing. Bo Wang: Conceptualization, Supervision, Funding acquisition, Validation, Project administration, Writing-original draft, Writing-review and editing. Jianfeng Yang: Formal analysis, Writing-review and editing. All authors read and approved the manuscript.

References

1. Chen H, Ginzburg VV, Yang J, Yang Y, Liu W, Huang Y, Du L, Chen B (2016) Thermal conductivity of polymer-based composites: fundamentals and applications. Prog Polym Sci 59:41–85

2. Chen Y, Hou X, Liao M, Dai W, Wang Z, Yan C, Li H, Lin CT, Jiang N, Yu J (2020) Constructing a "pea-pod-like" alumina-graphene binary architecture for enhancing thermal conductivity of epoxy composite. Chem Eng J 381:122690

3. Zeng X, Sun J, Yao Y, Sun R, Xu JB, Wong CP (2017) A combination of boron nitride nanotubes and cellulose nanofibers for the preparation of a nanocomposite with high thermal conductivity. ACS Nano 11:5167–5178

4. Wang ZY, Zhou XN, Li ZX, Xu SS, Hao LC, Zhao JP, Wang B, Yang JF, Ishizaki K (2022) Enhanced thermal conductivity of epoxy composites by constructing thermal conduction networks via adding hybrid alumina filler. Polym Compos 43:483–492

5. Yao Y, Zhu X, Zeng X, Sun R, Xu JB, Wong CP (2018) Vertically aligned and interconnected SiC nanowire networks leading to significantly enhanced thermal conductivity of polymer composites. ACS Appl Mater Interfaces 10:9669–9678

6. Song SH, Park KH, Kim BH, Choi YW, Jun GH, Lee DJ, Kong BS, Paik KW, Jeon S (2013) Enhanced thermal conductivity of epoxy-graphene composites by using non-oxidized graphene flakes with non-covalent functionalization. Adv Mater 25:732–737

7. Han Z, Fina A (2011) Thermal conductivity of carbon nanotubes and their polymer nanocomposites: a review. Prog Polym Sci 36:914–944

8. Kim K, Ju H, Kim J (2016) Vertical particle alignment of boron nitride and silicon carbide binary filler system for thermal conductivity enhancement. Compos Sci Technol 123:99–105

9. Shen D, Zhan Z, Liu Z, Cao Y, Zhou L, Liu Y, Dai W, Nishimura K, Li C, Lin CT, Jiang N, Yu J (2017) Enhanced thermal conductivity of epoxy composites filled with silicon carbide nanowires. Sci Rep 7:2606

10. Dai W, Yu J, Liu Z, Wang Y, Song Y, Lyu J, Bai H, Nishimura K, Jiang N (2015) Enhanced thermal conductivity and retained electrical insulation for polyimide composites with SiC nanowires grown on graphene hybrid fillers. Compos Part A Appl Sci Manuf 76:73–81

11. Wang B, Zhang H, Phuong HT, Jin F, Yang JF, Ishizaki K (2015) Gas permeability and adsorbability of the glass-bonded porous silicon carbide ceramics with controlled pore size. Ceram Int 41:2279–2285

12. Li B, Zhong WH (2011) Review on polymer/graphite nanoplatelet nanocomposites. J Mater Sci 46:5595–5614

13. Feng C, Ni H, Chen J, Yang W (2016) Facile method to fabricate highly thermally conductive graphite/PP composite with network structures. ACS Appl Mater Interfaces 8:19732–19738

14. Jung H, Yu S, Bae NS, Cho SM, Kim RH, Cho SH, Hwang I, Jeong B, Ryu JS, Hwang J, Hong SM, Koo CM, Park C (2015) High through-plane thermal conduction of gaphene nanoflake filled polymer composites melt-processed in an L-shape kinked tube. ACS Appl Mater Interfaces 7:15256–15262

15. Zhao W, Kong J, Liu H, Zhuang Q, Gu J, Guo Z (2016) Ultra-high thermally conductive and rapid heat responsive poly(benzobisoxazole) nanocomposites with self-aligned graphene. Nanoscale 8:19984–19993

16. Yan Q, Alam FE, Gao J, Dai W, Tan X, Lv L, Wang J, Zhang H, Chen D, Nishimura K, Wang L, Yu J, Lu J, Sun R, Xiang R, Maruyama S, Zhang H, Wu S, Jiang N, Lin CT (2021) Soft and self-adhesive thermal interface materials based on vertically aligned, covalently bonded graphene nanowalls for efficient microelectronic cooling. Adv Funct Mater 31:2104062

17. Wei Z, Xie W, Ge B, Zhang Z, Yang W, Xia H, Wang B, Jin H, Gao N, Shi Z (2020) Enhanced thermal conductivity of epoxy composites by constructing aluminum nitride honeycomb reinforcements. Compos Sci Technol 199:108304

18. Hao LC, Li ZX, Sun F, Ding K, Zhou XN, Song ZX, Shi ZQ, Yang JF, Wang B (2019) High-performance epoxy composites reinforced with three-dimensional Al_2O_3ceramic framework. Compos Part A Appl Sci Manuf 127:105648

19. Yao Y, Sun J, Zeng X, Sun R, Xu JB, Wong CP (2018) Construction of 3D skeleton for polymer composites achieving a high thermal conductivity. Small 14:1704044

20. Zhang P, Ding X, Wang Y, Gong Y, Zheng K, Chen L, Tian X, Zhang X (2019) Segregated double network enabled effective electromagnetic shielding composites with extraordinary electrical insulation and thermal conductivity. Compos Part A Appl Sci Manuf 117:56–64

21. Chen J, Huang X, Sun B, Jiang P (2019) Highly thermally conductive yet electrically insulating polymer/boron nitride nanosheets nanocomposite films for improved thermal management capability. ACS Nano 13:337–345

22. Han J, Du G, Gao W, Bai H (2019) An anisotropically high thermal conductive boron nitride/epoxy composite based on nacre-mimetic 3D network. Adv Funct Mater 29:1900412

23. Chen J, Huang X, Zhu Y, Jiang P (2017) Cellulose nanofiber supported 3D interconnected BN nanosheets for epoxy nanocomposites with ultrahigh thermal management capability. Adv Funct Mater 27:1604754

24. Lian G, Tuan CC, Li L, Jiao S, Wang Q, Moon KS, Cui D, Wong CP (2016) Vertically aligned and interconnected graphene networks for high thermal conductivity of epoxy composites with ultralow loading. Chem Mater 28:6096–6104

25. Shtein M, Nadiv R, Buzaglo M, Kahil K, Regev O (2015) Thermally conductive graphene-polymer composites: size, percolation, and synergy effects. Chem Mater 27:2100–2106

26. Zeng X, Yao Y, Gong Z, Wang F, Sun R, Xu J, Wong CP (2015) Ice-templated assembly strategy to construct 3D boron nitride nanosheet networks in polymer composites for thermal conductivity

improvement. Small 11:6205–6213

27. Hu J, Huang Y, Yao Y, Pan G, Sun J, Zeng X, Sun R, Xu JB, Song B, Wong CP (2017) Polymer composite with improved thermal conductivity by constructing a hierarchically ordered three-dimensional interconnected network of BN. ACS Appl Mater Interfaces 9:13544–13553

28. Fang H, Bai SL, Wong CP (2017) Thermal, mechanical and dielectric properties of fexible BN foam and BN nanosheets reinforced polymer composites for electronic packaging application. Compos Part A Appl Sci Manuf 100:71–80

29. Huang X, Jiang P, Tanaka T (2011) A review of dielectric polymer composites with high thermal conductivity. IEEE Electr Insul M 27:8–16

30. Huang X, Zhi C, Jiang P, Golberg D, Bando Y, Tanaka, T (2013) Polyhedral oligosilsesquioxane-modified boron nitride nanotube based epoxy nanocomposites: an ideal dielectric material with high thermal conductivity. Adv Funct Mater 23:1824–1831

31. Zhi C, Bando Y, Terao T, Tang C, Kuwahara H, Golberg D (2009) Boron nanotube-polymer composites: towards thermoconductive, electrically insulating polymeric composites with boron nitride nanotubes as fillers. Adv Funct Mater 19:1857–1862

32. Xue Y, Zhou X, Zhan T, Jiang B, Guo Q, Fu X, Shimamura K, Xu Y, Mori T, Dai P, Bando Y, Tang C, Golberg D (2018) Densely interconnected porous BN frameworks for multifunctional and isotropically thermoconductive polymer composites. Adv Funct Mater 28:1801205

33. Xue Y, Dai P, Zhou M, Wang X, Pakdel A, Zhang C, Weng Q, Takei T, Fu X, Popov ZI, Sorokin PB, Tang C, Shimamura K, Bando Y, Golberg D (2017) Multifunctional superelastic foam-like boron nitride nanotubular cellular-network architectures. ACS Nano 11:558–568

34. Fan TX, Chow SK, Zhang D (2009) Biomorphic mineralization: from biology to materials. Prog Mater Sci 54:542–659

35. Yin Z, Hannard F, Barthelat F (2019) Impact-resistant nacre-like transparent materials. Science 364:1260–1263

36. Erb RM, Libanori R, Rothfuchs N, Studart AR (2012) Composites reinforced in three dimensions by using low magnetic fields. Science 335:199–204

37. Billaud J, Bouville F, Magrini T, Villevieille C, Studart AR (2016) Magnetically aligned graphite electrodes for high-rate performance Li-ion batteries. Nat Energy 1:16097

38. Zhang JF, Zhou XN, Huang X, Hao LC, Zhi Q, Li ZX, Hou BQ, Yang JF, Wang B, Ishizaki K (2019) Biomorphic cellular silicon carbide nanocrystal-based ceramics derived from wood for use as thermally stable and lightweight structural materials. ACS Appl Nano Mater 2:7051–7060

39. Fernandes M, Cattoen X, de Zea Bermudez V, Chi Man MW (2011) Solvent-controlled morphology of lamellar silsesquioxanes: from platelets to microsponges. CrystEngComm 13:1410–1415

40. Foygel M, Morris RD, Anez D, French S, Sobolev VL (2005) Theoretical and computational studies of carbon nanotube composites and suspensions: electrical and thermal conductivity. Phys Rev B 71:104201

41. Yu A, Ramesh P, Itkis ME, Bekyarova E, Haddon RC (2007) Graphite nanoplatelet-epoxy composite thermal interface materials. J Phys Chem C 111:7565–7569

42. Yin L, Zhou X, Yu J, Wang H, Ran C (2016) Fabrication of a polymer composite with high thermal conductivity based on sintered silicon nitride foam. Compos Part A Appl Sci Manuf 90:626–632

43. Wu Y, Ye K, Liu Z, Wang B, Yan C, Wang Z, Lin CT, Jiang N, Yu J (2019) Cotton candy-templated fabrication of three-dimensional ceramic pathway within polymer composite for enhanced thermal conductivity. ACS Appl Mater Interfaces 1:44700–44707

44. Ma AJ, Li H, Chen W, Hou Y (2013) Improved thermal conductivity of silicon carbide/carbon fiber/epoxy resin composites. Polym Plast Technol Eng 52:295–299

45. Kim K, Kim M, Kim J, Kim J (2015) Magnetic filler alignment of paramagnetic Fe_3O_4 coated SiC/epoxy composite for thermal conductivity improvement. Ceram Int 41:12280–12287

46. An F, Li X, Min P, Liu P, Jiang ZG, Yu ZZ (2018) Vertically aligned high-quality graphene foams for anisotropically conductive polymer composites with ultrahigh through-plane thermal conductivities. ACS Appl Mater Interfaces 10:17383–17392

47. Kusunose T, Yagi T, Firozc SH, Sekinod T (2013) Fabrication of epoxy/silicon nitridenanowire composites and evaluation of their thermal conductivity. J Mater Chem A 1:3440–3445

48. Hu Y, Du G, Chen N (2016) A novel approach for Al_2O_3/epoxy composites with high strength and thermal conductivity. Compos Sci Technol 124:36–43

49. Kim K, Kim J (2016) Magnetic aligned AlN/epoxy composite for thermal conductivity enhancement at low filler content. Compos B Eng 93:67–74

50. Wu H, Kessler MR (2015) Multifunctional cyanate ester nanocomposites reinforced by hexagonal boron nitride after noncovalent biomimetic functionalization. ACS Appl Mater Interfaces 7:5915–5926

51. Turner PS (1946) Thermal-expansion stresses in reinforced plastics. J Res Natl Bur Stand 37:239–250

52. Kerner EH (1956) The elastic and thermo-elastic properties of composite media. Proc Phys Soc B 69:808–813

53. Shahil KMF, Balandin AA (2012) Graphene-multilayer graphene nanocomposites as highly efficient thermal interface materials. Nano Lett 12:861–867

54. Zhou S, Chen Y, Zou H, Liang M (2013) Thermally conductive composites obtained by flake graphite filling immiscible polyamide 6/polycarbonate blends. Thermochim Acta 566:84–91

55. Park SJ, Jin FL (2004) Thermal stabilities and dynamic mechanical properties of sulfone-containing epoxy resin cured with anhydride. Polym Degrad Stab 86:515–520

56. Wang WS, Chen HS, Wu YW, Tsai TY, Chen-Yang YW (2008) Properties of novel epoxy/clay nanocomposites prepared with a reactive phosphorus-containing organoclay. Polymer 49:4826–4836

57. Cao Y, Feng J, Wu P (2010) Preparation of organically dispersible graphene nanosheet powders through a lyophilization method and their poly(lactic acid) composites. Carbon 48:3834–3839

58. Wang X, Gong LX, Tang LC, Peng K, Pei YB, Zhao L, Wu LB, Jiang JX (2015) Temperature dependence of creep and recovery behaviors of polymer composites filled with chemically reduced graphene oxide. Compos Part A Appl Sci Manuf 69:288–298

59. Wang J, Liu D, Li Q, Chen C, Chen Z, Naebe M, Song P, Portehault D, Garvey CJ, Golberg D, Lei W (2021) Nacre-bionic anocomposite membrane for efficient in-plane dissipation heat harvest under high temperature. J Materiomics 7:219–225

60. Chen W, Liu P, Min L, Zhou Y, Liu Y, Wang Q, Duan W (2018) Non-covalently functionalized graphene oxide-based coating to enhance thermal stability and flame retardancy of PVA film. Nano-Micro Lett 10:39

Figures
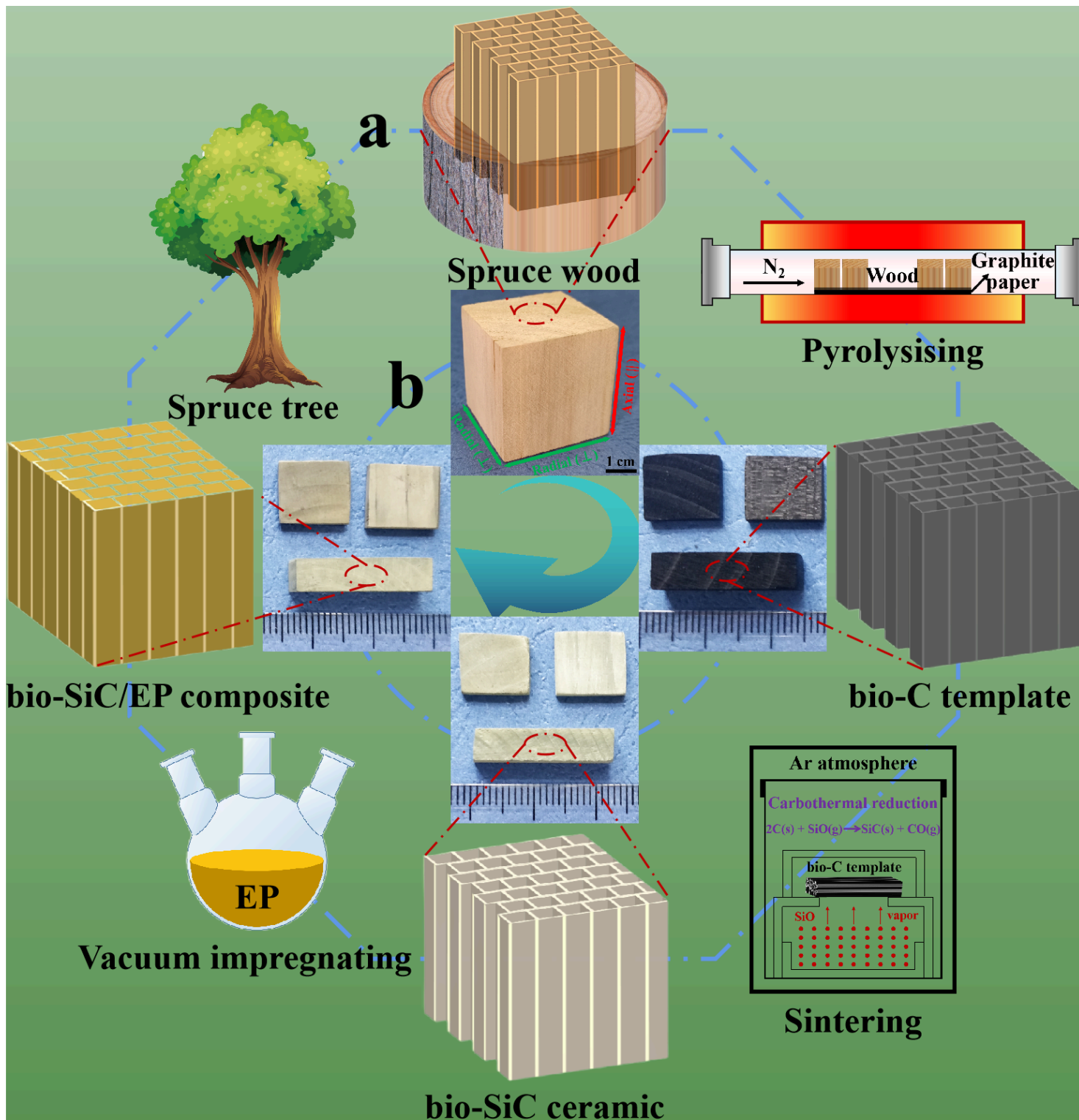
Figure 1

a Schematic diagram of the overall fabrication process ofbio-SiC/EP composite. **b** Digital images of spruce wood, bio-C templates, bio-SiC ceramicsand bio-SiC/EP composites.

The wood-carbon-ceramic-composite'sdesign idea and straight forward top-down preparation procedure of the bio-SiC/EP composites are illustrated in Fig. 1a. We choose spruce wood as the rawmaterial due to its unusual structure, consisting of anisotropic and highly dense elongated microchannels. The

original natural wood can be easily transformed into biomorphic carbon (bio-C) template by carbonization at high temperature. After that, the porous bio-SiC ceramic wassynthesized by the carbothermal reduction (CR)reaction of bio-C template on the basis ofthe equation: $2C(s) + SiO(g) \rightarrow SiC(s) + CO(g)$. Subsequently, liquid EP was penetrated into the functionalized 3D bio-SiC framework and thenthermal curing to form dense bio-SiC/EP composite with "brick and mortar" architecture. Different from loosely contacted 3D filler networks, a monolith of a 3D bio-SiC network was fabricated by our approach, in which heat energy can move rapidly through the high-quality and continuous bio-SiC microchannels. Therefore, we expect to observe extraordinary thermal properties of bio-SiC ceramic and bio-SiC/EP composite.

Figure 2

Microstructure of anisotropic bio-SiC/EP composite. **a**Micro-CT images of bio-SiC/EP composite. Cross-section images of **b, c**axial direction and **d, e** radial direction of bio-SiC/EP composite. Corresponding top-view SEM images of **f** bio-C template, **g** bio-SiC ceramic and **h** bio-SiC/EP composite with "brick and mortar" architecture. **i** EDS mapping image of (h). Corresponding left-view SEM images of **j** bio-C

template, **k** bio-SiC ceramic and **l** bio-SiC/EP composite with "cross-lamellar" architecture. **m** EDS mapping image of (l).
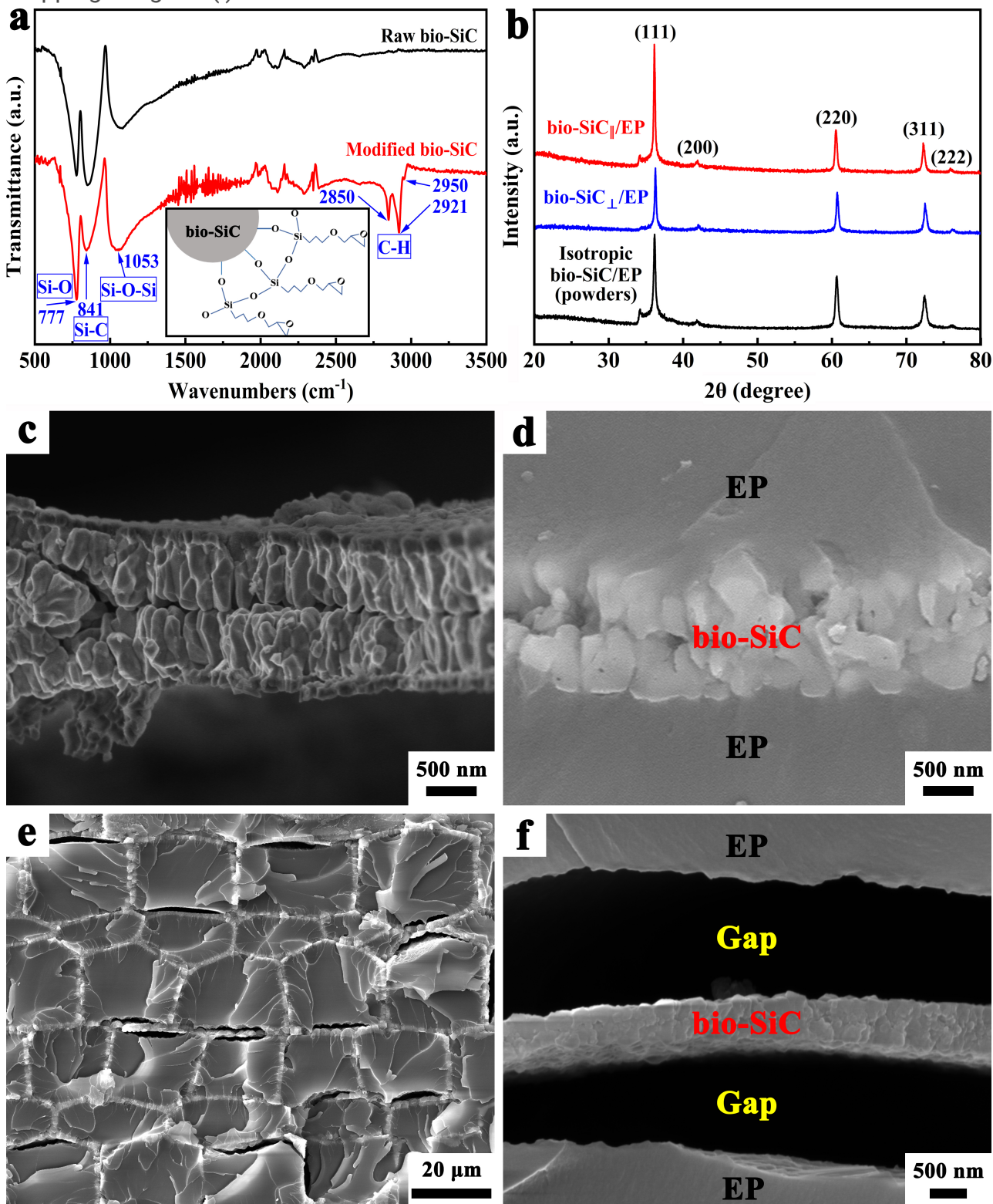

Figure 3

Phase identifications and SEM images of bio-SiC ceramics and bio-SiC/EP composites. **a** FTIR spectra of raw bio-SiC and modified bio-SiC ceramics. **b** XRD patterns of bio-SiC/EP composites. **c** SEM image of

bio-SiC ceramic. **d** SEM image of the interface between modified bio-SiC and EP. **e** SEM image of unmodified bio-SiC/EP composite. **f** SEM image of the interface between unmodified bio-SiC and EP.
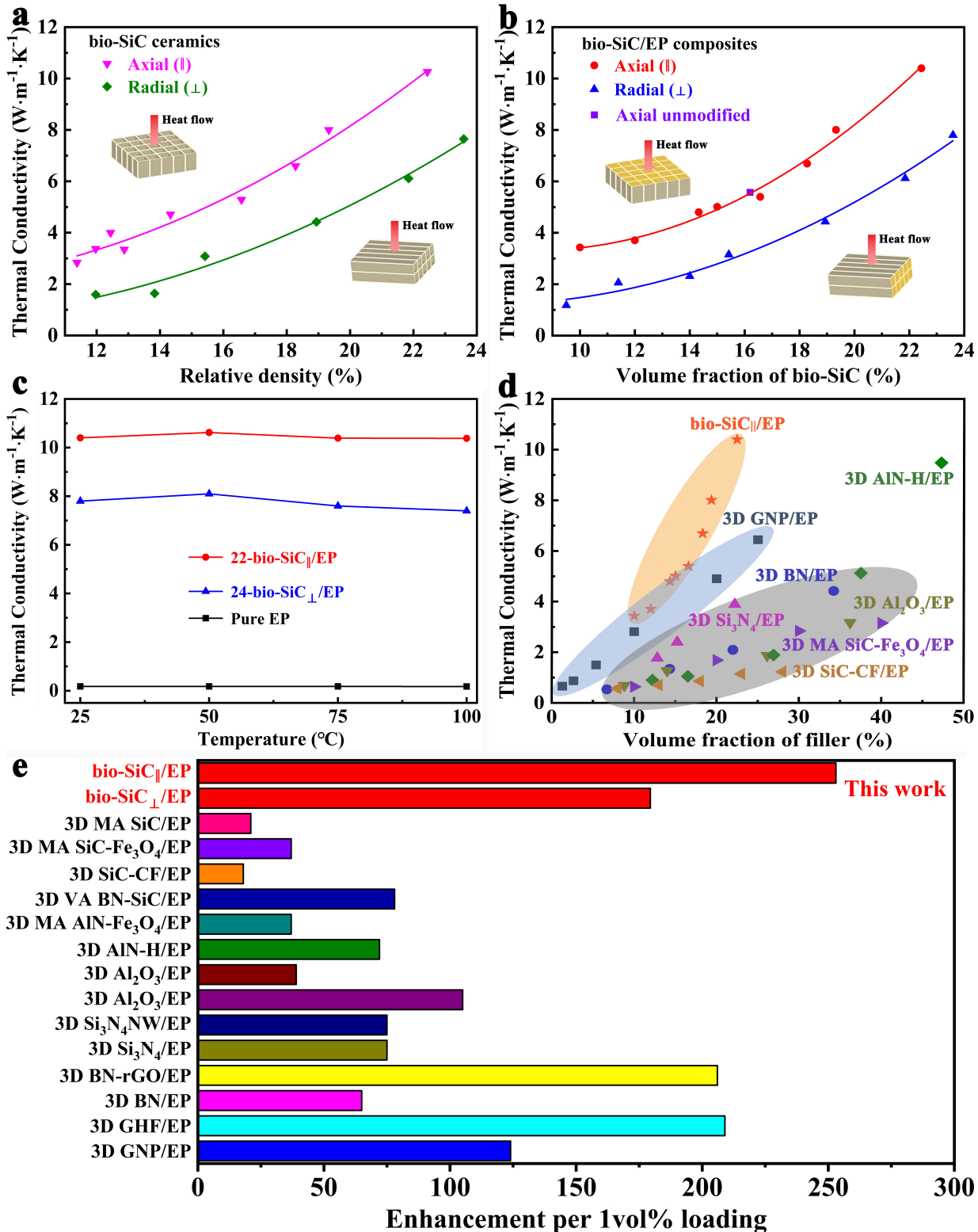
Figure 4

TC of bio-SiC ceramics and bio-SiC/EP composites. **a** Anisotropic TC of bio-SiC ceramics as a function of relative density. **b** Anisotropic TC of bio-SiC/EP composites with different bio-SiC loadings. **c** TC of 22-bio-SiC$_{\parallel}$/EP composite, 24-bio-SiC$_{\perp}$/EP composite and pure EP as a function of temperature.

Comparison of **d** TC and **e** TC enhancement efficiency of bio-SiC/EP composites and other epoxy composites reported previously.
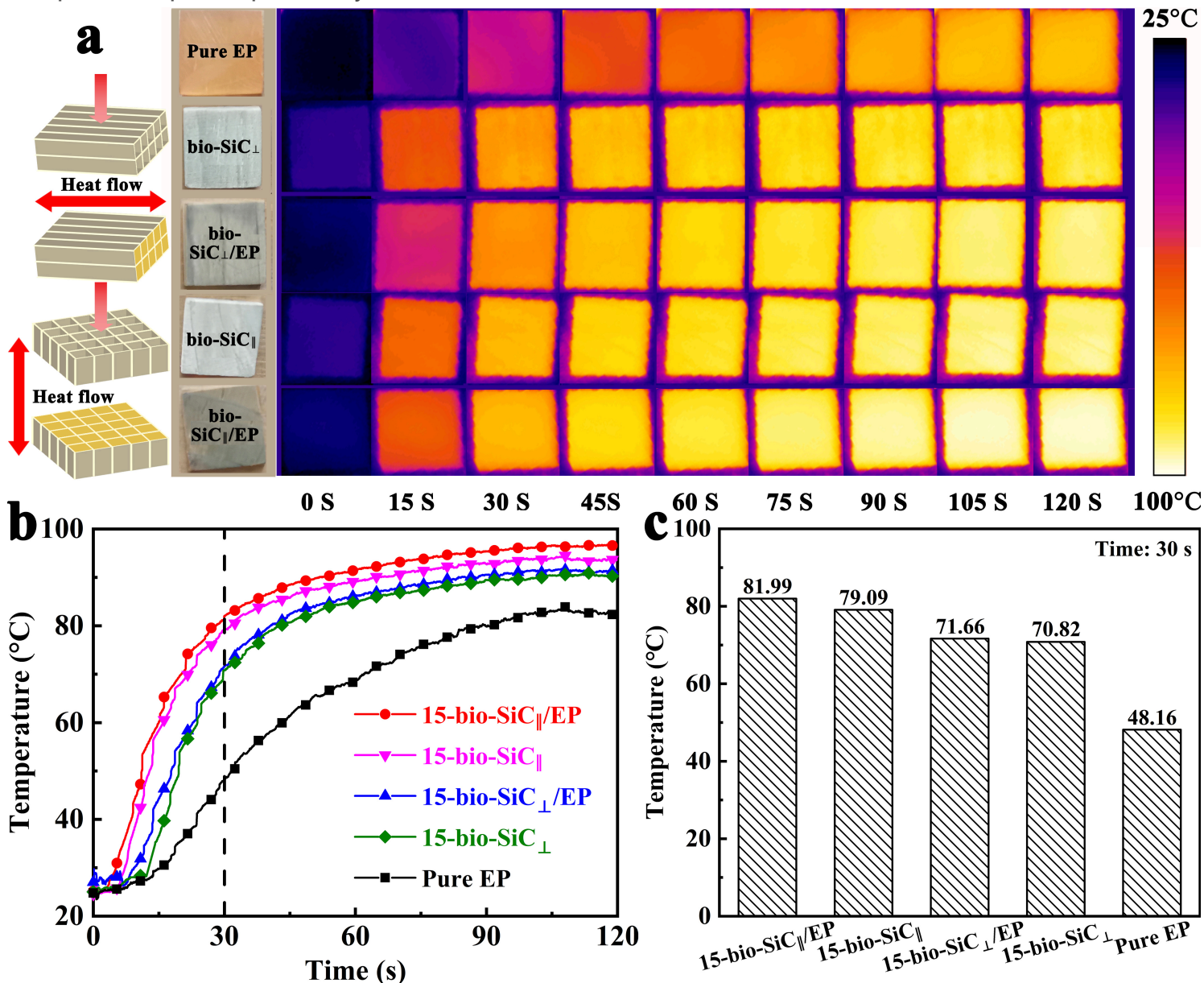
Figure 5

Pure EP, 15-bio-SiC ceramics and 15-bio-SiC/EP composites in thermal management applications. **a** Infrared thermal images and **b** top surface temperature at different heating times. **c** Top surface temperatures at 30 s.
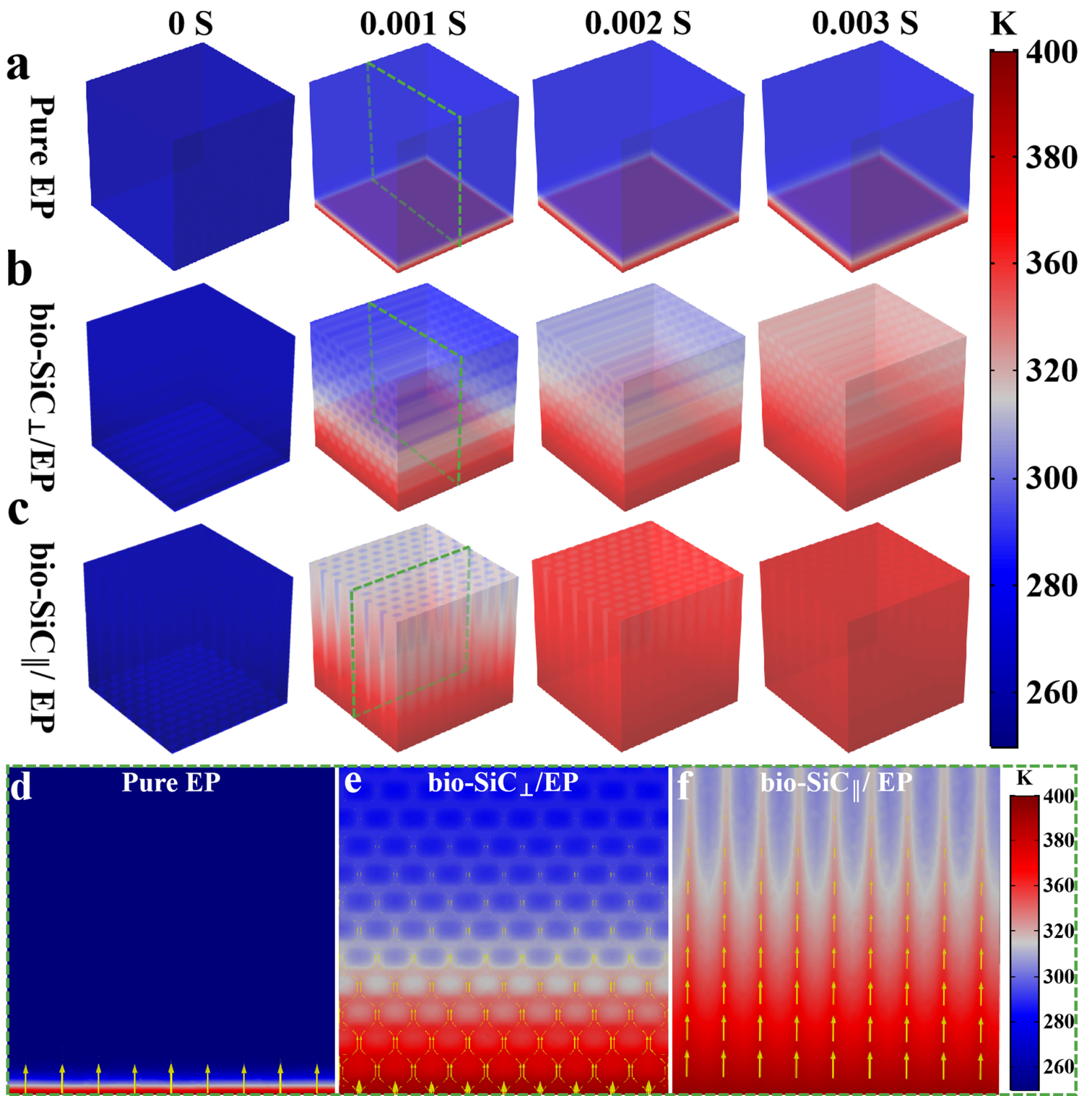
Figure 6

Thermal conduction behavior simulated by finite element simulation. Temperature distribution of **a** pure EP, **b** 20-bio-SiC$_\perp$/EP composite and **c** 20-bio-SiC$_\parallel$/EP composite. Heat flux arrows of **d** the section of (a) at 0.001 s, **e** the section of (b) at 0.001 s and **f** the section of (c) at 0.001 s.
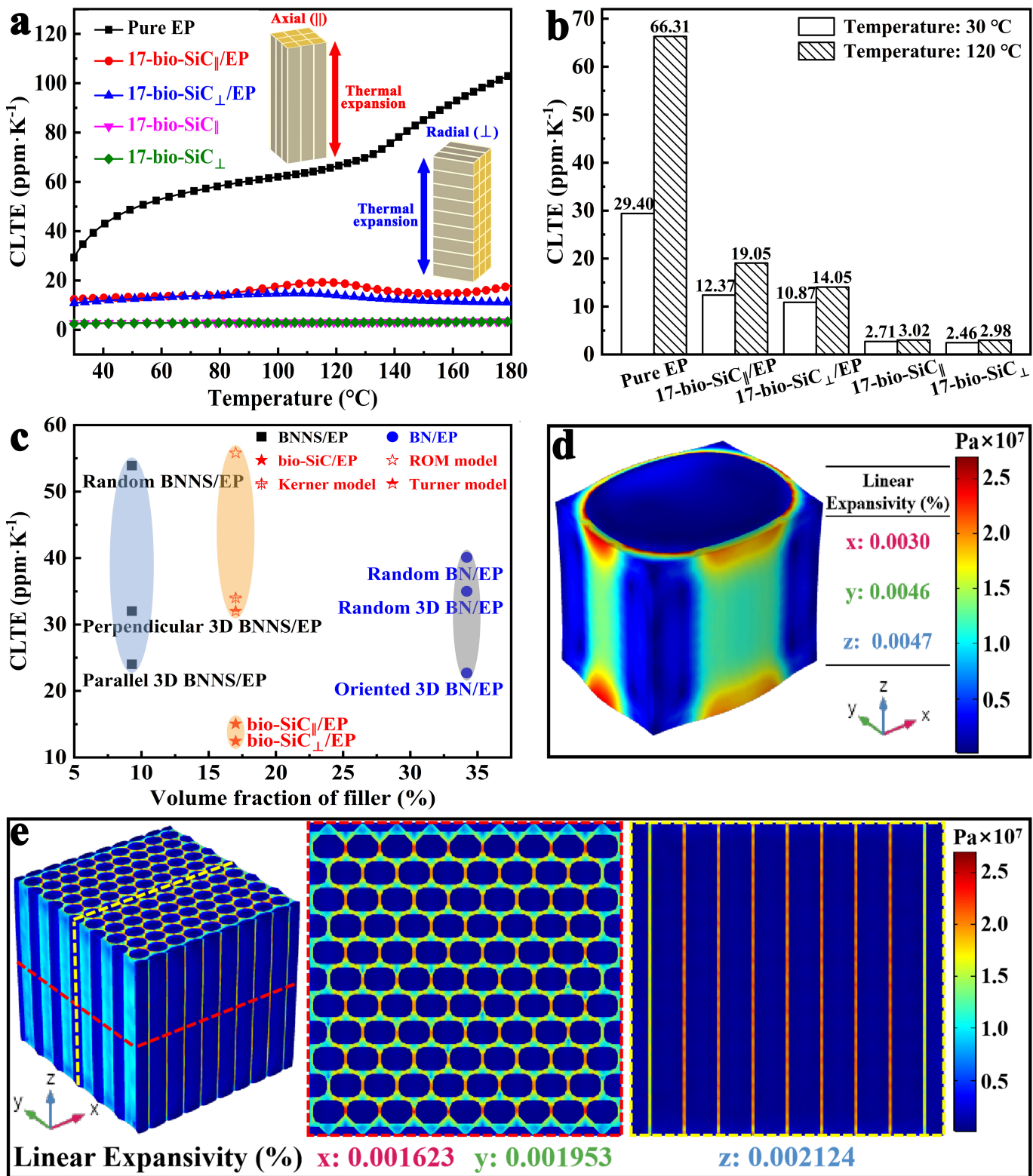
Figure 7

CLTE of pure EP, 17-bio-SiC ceramics and 17-bio-SiC/EP composites. **a** CLTE curves as a function of temperature. **b** CLTE values at 30 and 120 °C. **c** Comparison of CLTE values of 17-bio-SiC/EP composites and other epoxy composites reported previously. Thermal expansion process simulated by finite element simulation. Distribution of thermal stress and linear expansivity of **d** a single unit and **e** multiple units with 20 vol% bio-SiC at 120 °C.
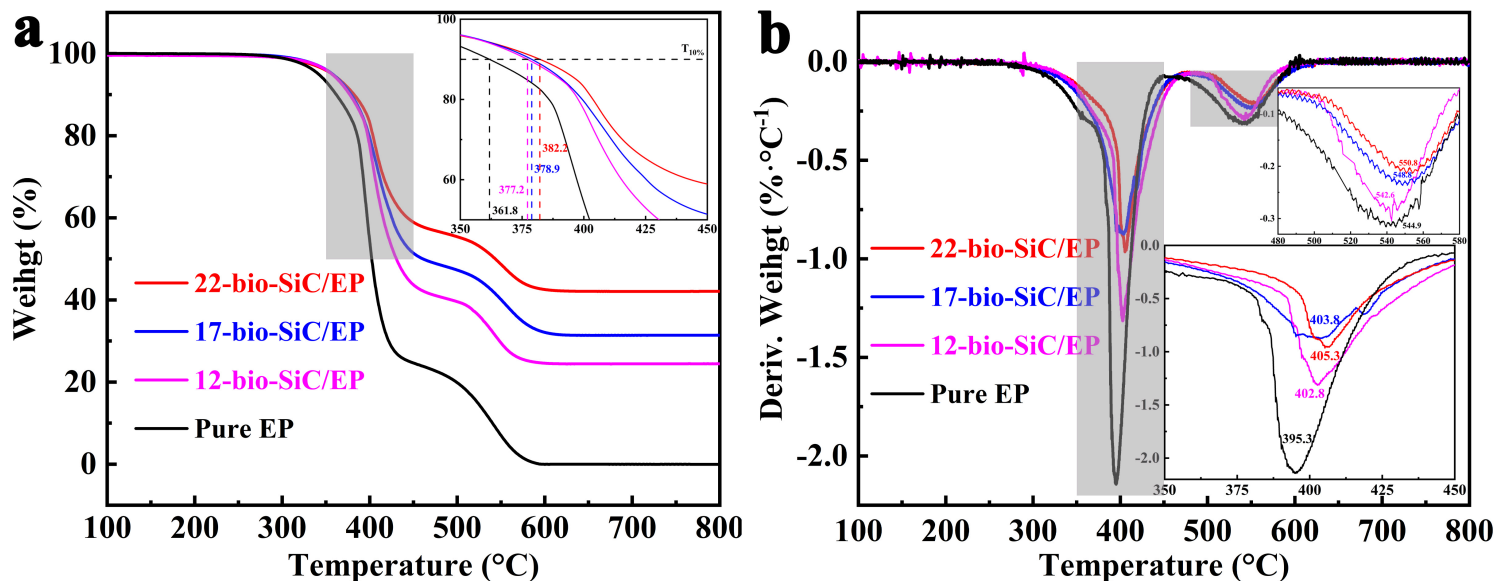
Figure 8

a TGA and **b** DTG curves of pure EP and bio-SiC/EP composites under air atmosphere.
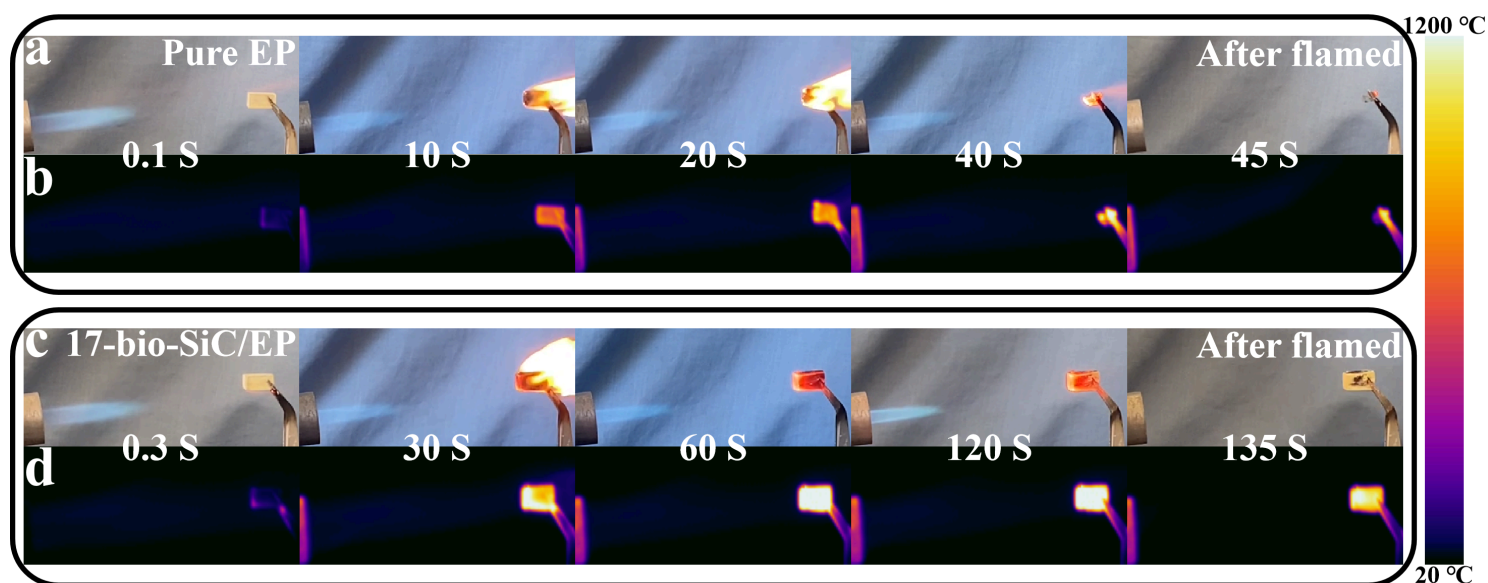

Figure 9

Anti-flaming performance of pure EP and 17-bio-SiC/EP composite. Snapshots of flame treatment of **a** pure EP and **c** 17-bio-SiC/EP composite at different burning times. Infrared thermal images of **b** pure EP and **d** 17-bio-SiC/EP composite at different burning times.
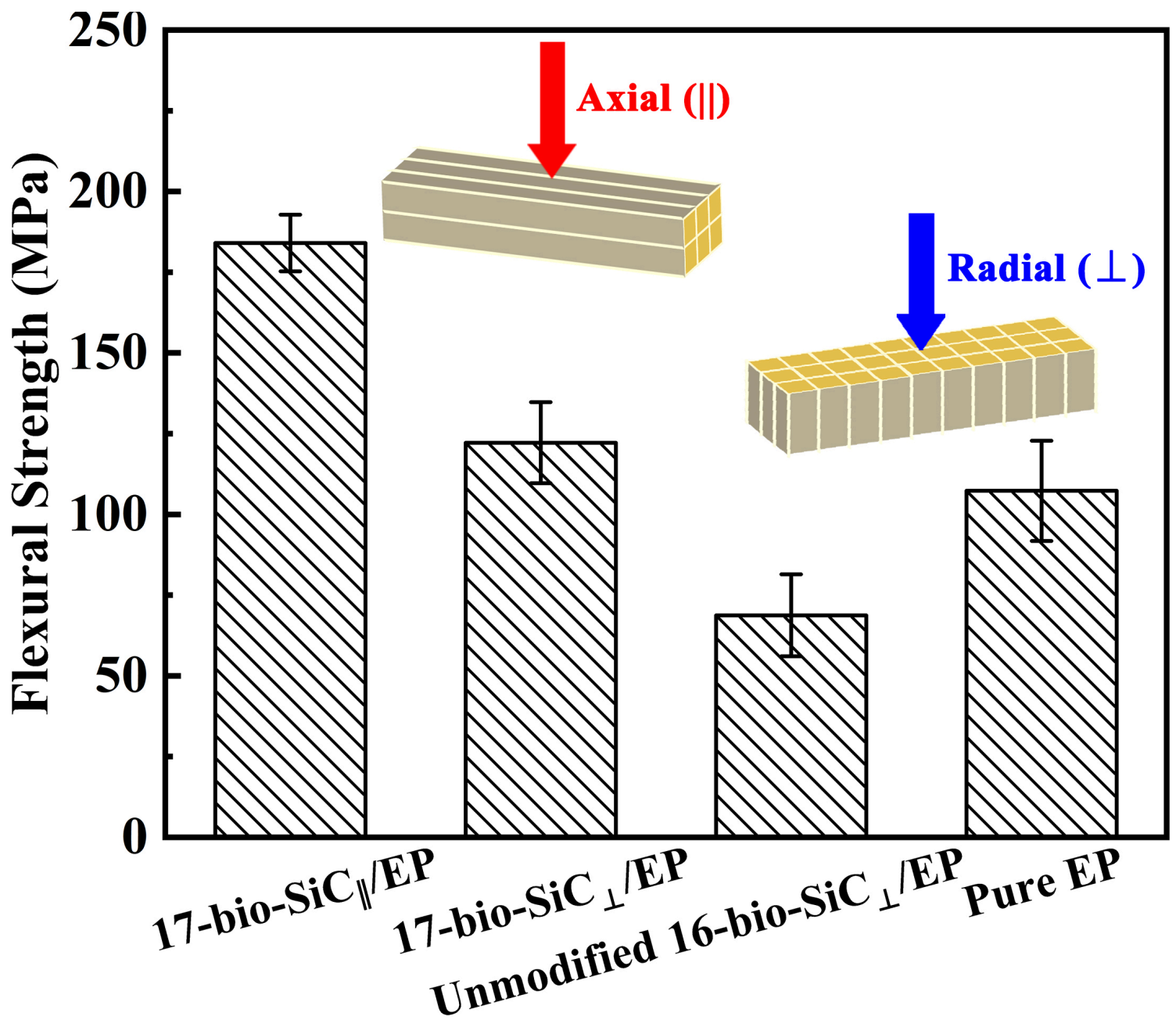
Figure 10

Flexural strengths of pure EP, unmodified 16-bio-SiC$_\perp$/EP composite and 17-bio-SiC/EP composites.

Supplementary Files

This is a list of supplementary files associated with this preprint. Click to download.

- Fig.S5a.gif
- Fig.S5b.gif
- Fig.S5c.gif
- SupportingInformation20221010.docx